PVP-Vol. 246/AMD-Vol. 143, New Methods in Transient Analysis
ASME 1992

COMPUTATION OF UNSTEADY INCOMPRESSIBLE FLOWS WITH THE STABILIZED FINITE ELEMENT METHODS: SPACE-TIME FORMULATIONS, ITERATIVE STRATEGIES AND MASSIVELY PARALLEL IMPLEMENTATIONS†

T. E. Tezduyar, M. Behr, S. Mittal, and A. A. Johnson
Department of Aerospace Engineering and Mechanics
Army High-Performance Computing Research Center and
Minnesota Supercomputer Institute
University of Minnesota
Minneapolis, Minnesota

ABSTRACT

We discuss the stabilized finite element computation of unsteady incompressible flows, with emphasis on the space-time formulations, iterative solution techniques and implementations on the massively parallel architectures such as the Connection Machines. The stabilization technique employed in this paper is the Galerkin/least-squares (GLS) method. The Deformable-Spatial-Domain/Stabilized-Space-Time (DSD/SST) formulation was developed for computation of unsteady viscous incompressible flows which involve moving boundaries and interfaces. In this approach, the stabilized finite element formulations of the governing equations are written over the space-time domain of the problem, and therefore the deformation of the spatial domain with respect to time is taken into account automatically. This approach gives us the capability to solve a large class of problems with free surfaces, moving interfaces, and fluid-structure and fluid-particle interactions. In the DSD/SST approach the frequency of remeshing is minimized to minimize the projection errors involved in remeshing and also to increase the parallelization potential of the computations. We present a new mesh moving scheme that minimizes the need for remeshing; in this scheme the motion of the mesh is governed by the modified equations of linear homogeneous elasticity. The implicit equation systems arising from the finite element discretizations are solved iteratively by using the GMRES search technique with the clustered element-by-element, diagonal and nodal-block-diagonal preconditioners. Formulations with diagonal and nodal-block-diagonal preconditioners have been implemented on the Connection Machines CM-200 and CM-5. We also describe a new mixed preconditioning method we developed recently, and discuss the extension of this method to totally unstructured meshes. This mixed preconditioning method is similar, in philosophy, to multi-grid methods, but does not need any intermediate grid levels, and therefore is applicable to unstructured meshes and is simple to implement. The application problems considered include various free-surface flows and simple fluid-structure interaction problems such as vortex-induced oscillations of a cylinder and flow past a pitching airfoil.

†This research was sponsored by NASA-JSC under grant NAG 9-449, by NSF under grant MSM-8796352, and by ALCOA foundation. Partial support for this work has also come from the Army Research Office contract number DAAL03-89-C-0038 with the Army High Performance Computing Research Center at the University of Minnesota.

1. INTRODUCTION

In this paper, we focus on finite element computation of unsteady incompressible flows governed by the Navier-Stokes equations. Although a great majority of the computations we report in this paper are based on the velocity-pressure formulation of the Navier-Stokes equations, we also report some Newtonian flow computations based on the velocity-pressure-stress formulation. It is of course not necessary for Newtonian flow computations to be based on the velocity-pressure-stress formulation; however, we consider these computations to be prelude to non-Newtonian flow computations, which would necessitate the stress tensor to be treated as a separate unknown.

Finite element computations based on the standard Galerkin formulation of incompressible flows can involve numerical instabilities due to the presence of advection terms in the governing equations, and due to using inappropriate combinations of interpolation functions to represent the velocity, pressure and stress fields. To stabilize the computations, in this paper, we use the Galerkin/least-squares (GLS) formulation [1]–[6]. This formulation is consistent in the sense that an exact solution still satisfies the stabilized formulation. Consequently, potential numerical oscillations are prevented without introducing excessive numerical diffusion (i.e., without "over-stabilizing") and therefore without compromising the accuracy of the solution. For unsteady flow computations based on the velocity-pressure formulation, the GLS formulation is implemented in a strict way by using a space-time finite element approach [3]–[5]. For computations based on the velocity-pressure-stress formulation, on the other hand, to avoid the high cost associated with the space-time technique, we implement the GLS formulation in a less strict way [7]. We achieve this by time-discretizing the time derivative of the weighting functions before the spatial discretization; this saves us from being forced into a space-time formulation.

A major challenge in computational fluid dynamics is how to handle moving boundaries and interfaces, such as free-surface flows, two-liquid flows, fluid-particle and fluid-structure interactions. In the DSD/SST (Deforming-Spatial-Domain/Stabilized-Space-Time) procedure [3]–[5], the GLS-stabilized formulation of the problem is written over the associated space-time domain. In this way, we automatically take into account the deformation of the spatial domain and also protect the

computations against numerical oscillations. The finite element interpolation functions are piecewise linear but discontinuous in time so that the fully discrete equations are solved one space-time slab at a time. In the DSD/SST approach, there is substantial freedom in the way we can move the mesh. We only need to remesh when it becomes necessary to do so to prevent unacceptable degrees of mesh distortion. By minimizing the frequency of remeshing, we can minimize the projection errors associated with remeshing, and increase the parallelization potential of the computations [7]. In this paper, we also employ a new mesh moving scheme that minimizes the need for remeshing. In this scheme the motion of the mesh is governed by the modified equations of linear homogeneous elasticity. The modification is achieved by dropping, in the computation of the stiffness matrix, the Jacobian of the transformation from the element domain to the physical domain. This is equivalent to introducing variable material properties to the equations of elasticity, with smaller elements having higher rigidity than the larger ones. This way smaller elements deform less, and the larger ones, by deforming more, take more responsibility in mesh motion by deformation. A similar mesh moving scheme can be found in [8].

To solve the large implicit equation systems resulting from the finite element discretization of realistic problems, especially those formulated in space-time and 3D domains, we use sophisticated preconditioning methods and massively parallel algorithms. In the CEBE (clustered element-by-element) preconditioning [9]–[10] the elements are merged into clusters of elements, and the preconditioners are constructed as series products of cluster level matrices. We attached our CEBE based iterative solver to all our finite element codes, in such a way that this solver is called just as easily and transparently as one calls a direct solver. In the CC (cluster companion) preconditioning [11] we first start with a "primary" mesh with different levels of clustering. For each level of clustering in this primary mesh, we define a "companion" mesh, such that each cluster of the primary mesh forms an element of the companion mesh. We define a CC preconditioner based on each companion mesh, such that there is a CC preconditioner associated with each CEBE preconditioner based on a certain level of clustering. This way, for each level of clustering, we obtain a CC preconditioner which we expect to have more inter-cluster coupling information than the associated CEBE preconditioner has. Conversely, the CEBE preconditioner can be expected to have more intra-cluster coupling information than the associated CC preconditioner has.

The idea behind the mixed CEBE/CC preconditioning [11] is that the CEBE and CC preconditioners complement each other, and therefore when they are mixed together they will result in better convergence rates. The mixing is currently implemented by using these two preconditioners alternately at each inner iteration of the GMRES method. The CEBE/CC preconditioning can be viewed as a multi-grid method without the intermediate grid levels. The preliminary results (see [11]) are quite promising. Our numerical tests, for 2D and 3D problems governed by the Poisson equation, demonstrate that the mixed CEBE/CC preconditioning results in convergence rates which are significantly better than the convergence rates obtained with the best of the CEBE and CC preconditioning methods. The details of the CEBE/CC method can be found in [11]; here we briefly describe the CEBE/CC strategy for totally unstructured meshes. Figure 1 shows two hypothetical meshes superimposed on each other: a fine primary mesh and a coarse mesh, both totally unstructured and arbitrary. In this case the clustering is achieved by distributing the elements of the fine mesh among the elements of the coarse mesh. Figure 1 also shows how a cluster of elements (marked in this figure with shaded areas) forms, in an approximate sense, an element of the coarse (companion) mesh.

In an effort to solve our large-scale problems by massively parallel computing, we have implemented almost all of our finite element formulations on the Connection Machines (CM-200 and CM-5) (see [7]). These initial implementations are based on the GMRES search technique and the diagonal and nodal-block-diagonal preconditioning methods. The next step will be the implementations based on the CEBE preconditioning and eventually the mixed CEBE/CC preconditioning. It is our belief that the mixed CEBE/CC preconditioning technique will be more easily parallelizable than the multi-grid methods.

We present several numerical examples, including those involving the dynamics of liquid drops and other free-surface flows, and flows past oscillating airfoils.

2. SPACE-TIME VELOCITY-PRESSURE FORMULATION

Consider a viscous, incompressible fluid occupying at an instant $t \in (0,T)$ a bounded region $\Omega_t \subset I\!R^{n_{sd}}$, with boundary Γ_t, where n_{sd} is the number of space dimensions. The velocity and pressure, $\mathbf{u}(\mathbf{x},t)$ and $p(\mathbf{x},t)$, are governed by the Navier-Stokes equations:

$$\rho\left(\frac{\partial \mathbf{u}}{\partial t} + \mathbf{u}\cdot\nabla\mathbf{u} - \mathbf{f}\right) - \nabla\cdot\boldsymbol{\sigma} = \mathbf{0} \qquad \text{on } \Omega_t \quad \forall t \in (0,T), \tag{1}$$

$$\nabla\cdot\mathbf{u} = 0 \qquad \text{on } \Omega_t \quad \forall t \in (0,T), \tag{2}$$

where ρ is the fluid density. The general body force $\mathbf{f}(\mathbf{x},t)$ can, e.g., represent the gravity. For a fluid with viscosity μ, the stress tensor $\boldsymbol{\sigma}$ can be decomposed into the isotropic and deviatoric parts:

$$\boldsymbol{\sigma} = -p\mathbf{I} + \mathbf{T}, \quad \mathbf{T} = 2\mu\boldsymbol{\varepsilon}(\mathbf{u}), \quad \boldsymbol{\varepsilon}(\mathbf{u}) = \frac{1}{2}\left(\nabla\mathbf{u} + (\nabla\mathbf{u})^T\right). \tag{3}$$

Both the Dirichlet- and Neumann-type boundary conditions are taken into account, represented as

$$\mathbf{u} = \boldsymbol{g} \qquad \text{on } (\Gamma_t)_{\boldsymbol{g}}, \tag{4}$$

$$\mathbf{n}\cdot\boldsymbol{\sigma} = \boldsymbol{h} \qquad \text{on } (\Gamma_t)_{\boldsymbol{h}}, \tag{5}$$

where $(\Gamma_t)_{\boldsymbol{g}}$ and $(\Gamma_t)_{\boldsymbol{h}}$ are complementary subsets of the boundary Γ_t. The initial condition consists of a specified divergence-free velocity field:

$$\mathbf{u}(\mathbf{x},0) = \mathbf{u}_0 \quad \text{on } \Omega_0. \tag{6}$$

In order to construct the finite element function spaces for the space-time method, we partition the time interval $(0,T)$ into subintervals $I_n = (t_n, t_{n+1})$, where t_n and t_{n+1} belong to an ordered series of time levels $0 = t_0 < t_1 < \cdots < t_N = T$. Let $\Omega_n = \Omega_{t_n}$ and $\Gamma_n = \Gamma_{t_n}$. We will define the space-time slab Q_n as the domain enclosed by the surfaces Ω_n, Ω_{n+1}, and P_n, where P_n is the surface described by the boundary Γ_t as t traverses I_n. As it is the case with Γ_t, surface P_n can be decomposed into $(P_n)_{\boldsymbol{g}}$ and $(P_n)_{\boldsymbol{h}}$ with respect to the type of boundary condition (Dirichlet or Neumann) being applied. For each space-time slab, we define the following finite element interpolation function spaces for the velocity and pressure:

$$(\mathcal{S}^h_{\mathbf{u}})_n = \left\{\mathbf{u}^h \mid \mathbf{u}^h \in \left[H^{1h}(Q_n)\right]^{n_{sd}}, \mathbf{u}^h = \boldsymbol{g}^h \quad \text{on } (P_n)_{\boldsymbol{g}}\right\}, \tag{7}$$

$$(\mathcal{V}^h_{\mathbf{u}})_n = \left\{\mathbf{u}^h \mid \mathbf{u}^h \in \left[H^{1h}(Q_n)\right]^{n_{sd}}, \mathbf{u}^h = \mathbf{0} \quad \text{on } (P_n)_{\boldsymbol{g}}\right\}, \tag{8}$$

$$(\mathcal{S}^h_p)_n = (\mathcal{V}^h_p)_n = \left\{p^h \mid p^h \in H^{1h}(Q_n)\right\}. \tag{9}$$

Over the element domain, the interpolation is constructed by using first-order polynomials in space and, depending on our choice, zeroth- or first-order polynomials in time. Globally, the interpolation functions are continuous in space but discontinuous in time. However, for two-liquid flows, the solution and variational function spaces for pressure should include the functions which are discontinuous across the interface.

The stabilized space-time formulation for deforming domains can be written as follows: given $(\mathbf{u}^h)^-_n$, find $\mathbf{u}^h \in (\mathcal{S}^h_{\mathbf{u}})_n$ and $p^h \in (\mathcal{S}^h_p)_n$ such that $\forall \mathbf{w}^h \in (\mathcal{V}^h_{\mathbf{u}})_n$, $\forall q^h \in (\mathcal{V}^h_p)_n$:

$$\int_{Q_n} \mathbf{w}^h \cdot \rho\left(\frac{\partial \mathbf{u}^h}{\partial t} + \mathbf{u}^h\cdot\nabla\mathbf{u}^h - \mathbf{f}\right) dQ + \int_{Q_n} \boldsymbol{\varepsilon}(\mathbf{w}^h) : \boldsymbol{\sigma}(p^h, \mathbf{u}^h) dQ$$

$$+ \int_{Q_n} q^h \rho \nabla \cdot \mathbf{u}^h dQ + \int_{\Omega_n} (\mathbf{w}^h)_n^+ \cdot \rho \left((\mathbf{u}^h)_n^+ - (\mathbf{u}^h)_n^- \right) d\Omega$$

$$+ \sum_{e=1}^{(n_{el})_n} \int_{Q_n^e} \tau \left[\rho \left(\frac{\partial \mathbf{w}^h}{\partial t} + \mathbf{u}^h \cdot \nabla \mathbf{w}^h \right) - \nabla \cdot \boldsymbol{\sigma}(q^h, \mathbf{w}^h) \right] \cdot \left[\rho \left(\frac{\partial \mathbf{u}^h}{\partial t} + \mathbf{u}^h \cdot \nabla \mathbf{u}^h - \mathbf{f} \right) - \nabla \cdot \boldsymbol{\sigma}(p^h, \mathbf{u}^h) \right] dQ$$

$$+ \sum_{e=1}^{(n_{el})_n} \int_{Q_n^e} \delta \nabla \cdot \mathbf{w}^h \rho \nabla \cdot \mathbf{u}^h dQ = \int_{(P_n)_{\boldsymbol{h}}} \mathbf{w}^h \cdot \boldsymbol{h}^h dP. \tag{10}$$

where

$$(\mathbf{u}^h)_n^{\pm} = \lim_{\varepsilon \to 0} \mathbf{u}(t_n \pm \varepsilon). \tag{11}$$

The solution to (10) is obtained sequentially for all the space-time slabs $Q_1, Q_2, \ldots, Q_{N-1}$. The computations start with

$$(\mathbf{u}^h)_0^+ = \mathbf{u}_0. \tag{12}$$

Remarks

1. In the variational formulation given by (10), the first three terms of the left hand side, together with the right hand side, constitute the standard Galerkin formulation of the problem. The fourth integral enforces, in a weak sense, the continuity of the velocity in time.

2. The fifth term in (10) is a least-squares addition to the formulation, and this term provides the necessary stability for advection-dominated flows in the presence of sharp boundary layers. The same term stabilizes the method against numerical oscillations which arise from certain combinations of interpolations for velocity and pressure, including the equal-order bilinear interpolation used in the current computations. See [3] for definition of the stabilization coefficient τ.

3. At high Reynolds numbers, the stability is improved by incorporating the sixth term into formulation (10); this is the least-squares term for the continuity equation. The coefficient δ is defined in [5].

3. VELOCITY-PRESSURE-STRESS FORMULATION

The physical problem under consideration is the same as the one defined by equations (1)–(6), i.e., Navier-Stokes equations for flows of incompressible Newtonian fluid. However, the $n_{sd}(n_{sd}+1)/2$ independent components of the deviatoric stress tensor $\mathbf{T}$ are treated as additional unknowns, and equation $(3)_2$ enters the variational formulation directly. The case of deforming domains is not covered here, so the subscripts denoting domain time level are dropped. The interpolation function spaces for the velocity, pressure and deviatoric stress tensor are given as:

$$\mathcal{S}_{\mathbf{u}}^h = \left\{ \mathbf{u}^h \mid \mathbf{u}^h \in \left[H^{1h}(\Omega) \right]^{n_{sd}}, \mathbf{u}^h = \boldsymbol{g}^h \quad \text{on } \Gamma_{\boldsymbol{g}} \right\}, \tag{13}$$

$$\mathcal{V}_{\mathbf{u}}^h = \left\{ \mathbf{u}^h \mid \mathbf{u}^h \in \left[H^{1h}(\Omega) \right]^{n_{sd}}, \mathbf{u}^h = \mathbf{0} \quad \text{on } \Gamma_{\boldsymbol{g}} \right\}, \tag{14}$$

$$\mathcal{S}_p^h = \mathcal{V}_p^h = \left\{ p^h \mid p^h \in H^{1h}(\Omega) \right\}, \tag{15}$$

$$\mathcal{S}_{\mathbf{T}}^h = \mathcal{V}_{\mathbf{T}}^h = \left\{ \mathbf{T}^h \mid \mathbf{T}^h \in \left[H^{1h}(\Omega) \right]^{n_{sd}(n_{sd}+1)/2} \right\}. \tag{16}$$

The velocity-pressure-stress formulation given here is an extension of Method II described in [6] to time-dependent problems, and can be written as follows: find $\mathbf{u}^h \in \mathcal{S}_{\mathbf{u}}^h$, $p^h \in \mathcal{S}_p^h$ and $\mathbf{T}^h \in \mathcal{S}_{\mathbf{T}}^h$ such that $\forall \mathbf{w}^h \in \mathcal{V}_{\mathbf{u}}^h$, $\forall q^h \in \mathcal{V}_p^h$ and $\forall \mathbf{S}^h \in \mathcal{V}_{\mathbf{T}}^h$

$$\int_{\Omega} \mathbf{w}^h \cdot \rho \left(\frac{\partial \mathbf{u}^h}{\partial t} + \mathbf{u}^h \cdot \nabla \mathbf{u}^h - \mathbf{f} \right) d\Omega$$

$$- \int_{\Omega} \nabla \cdot \mathbf{w}^h p^h d\Omega + \int_{\Omega} \boldsymbol{\varepsilon}(\mathbf{w}^h) : \mathbf{T}^h d\Omega$$

$$+ \frac{1}{2\nu} \int_{\Omega} \mathbf{S}^h : \mathbf{T}^h d\Omega - \int_{\Omega} \mathbf{S}^h : \boldsymbol{\varepsilon}(\mathbf{u}^h) d\Omega + \int_{\Omega} q^h \rho \nabla \cdot \mathbf{u}^h d\Omega$$

$$+ \sum_{e=1}^{n_{el}} \int_{\Omega^e} \tau \left[\rho \left(\frac{\partial \mathbf{w}^h}{\partial t} + \mathbf{u}^h \cdot \nabla \mathbf{w}^h \right) + \nabla q^h - \nabla \cdot \mathbf{S}^h \right] \cdot \left[\rho \left(\frac{\partial \mathbf{u}^h}{\partial t} + \mathbf{u}^h \cdot \nabla \mathbf{u}^h - \mathbf{f} \right) + \nabla p^h - \nabla \cdot \mathbf{T}^h \right] d\Omega$$

$$+ \sum_{e=1}^{n_{el}} \int_{\Omega^e} \alpha 2\nu \left[\frac{1}{2\nu} \mathbf{S}^h - \boldsymbol{\varepsilon}(\mathbf{w}^h) \right] : \left[\frac{1}{2\nu} \mathbf{T}^h - \boldsymbol{\varepsilon}(\mathbf{u}^h) \right] d\Omega$$

$$+ \sum_{e=1}^{n_{el}} \int_{\Omega^e} \delta \nabla \cdot \mathbf{w}^h \rho \nabla \cdot \mathbf{u}^h d\Omega = \int_{\Gamma_{\boldsymbol{h}}} \mathbf{w}^h \cdot \boldsymbol{h}^h d\Gamma. \tag{17}$$

Remarks

4. Aside from stabilization terms described in Section 2, the formulation given by (17) includes a least-squares form of the constitutive equation (3). Consequently, this formulation can be applied in conjunction with arbitrary combinations of interpolation functions for all variables, including presently employed equal-order bilinear combination.

5. Definitions of the coefficients τ, δ and α, as well as stability proof and error analysis for the steady-state case are given in [6].

6. In the computations that follow, formulation (17) has been discretized in time with the Crank-Nicholson scheme. The use of discontinuous Galerkin discretization (space-time method) is also planned.

7. The time derivative of the velocity weighting function represents the variation of the time derivative of the velocity itself. For example, in the case of space-time method, this term is the true time derivative of the weighting function. On the other hand, in the case of Euler-type time discretization with time step Δt, the term $\partial \mathbf{u}^h / \partial t$ is replaced by $(\mathbf{u}_{n+1}^h - \mathbf{u}_n^h)/\Delta t$, with $\mathbf{u}_n^h$ known, and thus the variation term becomes $\mathbf{w}^h / \Delta t$.

4. NUMERICAL EXAMPLES

Viscous drop falling in a viscous fluid

In this axisymmetric simulation, gravity is applied to two different fluids which causes the heavier fluid (drop) to fall and deform until terminal velocity and shape are reached. Surface tension is accounted for. At terminal velocity, the Reynolds number is 105, the Weber number is 5.51, and the drag coefficient is 1.61. Shown in Figure 2 is the drop at 5 equally spaced instants throughout the simulation. Also shown is an iso-surface of the vorticity and two iso-surfaces of the stream function. The finite element mesh consist of 8,151 nodes and 7,865 elements. The simulation was performed on a CM-5 supercomputer. At each non-linear iteration within each time step, approximately 48,000 equations are solved simultaneously using the GMRES technique with a diagonal preconditioner. To follow the motion of the drop as it falls, the entire finite element mesh translates together with the drop so that the center of gravity of the drop stays at the same location relative to the mesh.

A new mesh moving scheme is used to deform the mesh as the drop changes its shape. In this mesh moving scheme, a linear, elastostatics problem is solved whenever the mesh from the previous time step or iteration needs to be deformed into a new one. The boundary conditions for this elastostatics problem are used to define the new, desired shape

of the domain, and then the interior nodes get distributed accordingly. The equation being solved is

$$\sigma^m_{ij,j} = 0 \quad \text{in } \Omega, \tag{18}$$

with $\boldsymbol{\sigma}^m$ defined as

$$\sigma^m_{ij} = C_{ijkl}\varepsilon^m_{kl}, \tag{19}$$

where C_{ijkl} are the fictitious Hookean elastic coefficients, and $\boldsymbol{\varepsilon}^m$ defined as

$$\varepsilon^m_{kl} = \frac{v^m_{i,j} + v^m_{j,i}}{2}, \tag{20}$$

where $\mathbf{v}^m$ denotes displacements of the nodes. To better preserve the structure of the original mesh in the high resolution regions, the smaller elements are made stiffer than the larger ones. The modification is achieved by dropping, in the computation of the stiffness matrix, the Jacobian of the transformation from the element domain to the physical domain. By doing so, the smaller elements become stiffer than the larger ones; and thus, retain their shapes better. In this problem, we control the distribution of the nodes at the interface to have equal spacing throughout time.

Vortex interaction with a free surface

In this free surface problem (see Figure 3), surface deformations are generated by a pair of vortices approaching the surface from below. The vortices create large surface deformations, and eventually the generated wave breaks. The problem was solved with 7,802 elements and 8,016 nodes. The 47,570 field equations and 15,437 mesh movements equations were solved on CM-5 using a GMRES technique with a diagonal preconditioner. The results we report here are preliminary and were obtained with no remeshing at all. However, it is quite clear that this is a problem in which we will need some remeshing once in a while. In fact, due to unacceptable level of mesh distortions, after the last frame in Figure 3, the simulation becomes unreliable. In future simulations, remeshing will be used to generate a new mesh when the current mesh gets too distorted.

Fountain

The space-time formulation is applied here to solve a problem involving dramatic deformation of the initial domain. A flow from a fountain is simulated by prescribing a unit vertical velocity at the lower (inflow) boundary of an initially rectangular 1.0×2.0 domain. Vertical slip condition is imposed at the side walls of the initial domain, while the topmost (outflow) boundary is left free. As the fluid enters the domain, it overflows the slip walls and falls down under the influence of unit gravity. The fluid is assumed to be inviscid, and the time step is taken as 0.05. Three finite element meshes and pressure fields from this simulation are shown in Figure 4. In this case, a new mesh is generated automatically every time the domain is deformed, and the solution is projected from the old mesh to the new one. The number of elements grows from the initial 614 to 2,126 at $t = 6.0$.

Sprinkler

Similarly to the preceding example, the space-time formulation is used here to simulate flow from a sprinkler-like configuration. A short vertical pipe 2.0 units long and 1.0 unit wide is located 0.5 units above a perpendicular plate blocking the flow of fluid from the pipe. The fluid enters at the upper end of the pipe with unit downward velocity. The vertical pipe walls, as well as the blocking plate, are assumed to permit slip along the surface. The fluid flows around the plate and proceeds downward under the influence of a unit gravity force. The viscosity of the fluid is 0.001, while the time step is taken as 0.01. In this problem the surface tension coefficient at the fluid interface is 0.001. Three finite element meshes and pressure fields are shown in Figure 5. As in the preceding problem, large deformation of the domain justifies regeneration of the finite element mesh at every time step. The element count increases from 780 to 1,840 at $t = 4.0$.

Flow past an oscillating airfoil at Reynolds number 1,000

Flow at Reynolds number 1,000 is forced past a NACA 0012 airfoil which is oscillating with a non-dimensional frequency of 1.0. The airfoil oscillates between angles of attack of 10 and 30 degrees. Shown in Figure 6 is the vorticity at various instances during the simulation. The simulation was performed on a CM-5 supercomputer. At each non-linear iteration within each time step, roughly 39,000 equations are solved simultaneously using the GMRES technique with a diagonal preconditioner. The movement of the airfoil is facilitated by deformations in the space-time domain; and thus, no remeshing was needed. The finite element mesh, which consists of 6,609 nodes and 6,460 elements, can be seen in Figure 7, at 10° and 30° angle of attack.

Vortex-induced vibrations of a cylinder in vertical direction

This problem represents a simple model of fluid-structure interaction. A cylinder mounted on lightly damped springs is allowed to move in the vertical direction in response to the fluid forces acting on it. The motion of the cylinder alters the vortex shedding mechanism of the cylinder significantly and leads to several interesting physical phenomena. A detailed numerical investigation of such an oscillator can be found in [5]. The motion of the cylinder is governed by the following equation:

$$\frac{\partial^2 Y}{\partial t^2} + 2\pi F_n \zeta \frac{\partial Y}{\partial t} + (\pi F_n)^2 Y = \frac{C_L}{M}. \tag{21}$$

Here Y represents the normalized vertical displacement of the cylinder. The displacement and the velocity of the cylinder are normalized by its radius and the free-stream velocity respectively. M is the non-dimensional mass/unit length of the cylinder, ζ is the structural damping coefficient associated with the system, and C_L denotes the lift coefficient for the cylinder. F_n is the reduced natural frequency of the spring-mass system and is defined as:

$$F_n = \frac{2 f_n a}{U}, \tag{22}$$

where a is the radius of the cylinder, U is the free stream velocity and f_n is the actual natural frequency of the system. In this problem, $F_n = 66/Re$, $M = 472.74$ and $\zeta = 3.3 \times 10^{-4}$. Results are presented for two different Reynolds numbers — 324 and 300. For both cases, the unsteady flow past a fixed cylinder at the respective Reynolds numbers is used as the initial condition. The time step for the computations is 1.0. The finite element mesh consists of 4,209 nodes and 4,060 elements. At each time step approximately 25,000 equations are solved using the GMRES technique. In both cases, as a result of the cylinder vibrations, the drag and the torque acting on the cylinder increase substantially while there is a decrease in the amplitude of the lift acting on the cylinder.

Reynolds number 324

For Reynolds number 324 the reduced natural frequency of the spring-mass system and the Strouhal number for flow past a fixed cylinder have very close values. As soon as the cylinder is released it starts oscillating with an amplitude that increases with time. Eventually, a temporally periodic solution is obtained. Figure 8 shows the time histories of the drag and lift coefficients and the normalized vertical displacement of the cylinder for the periodic solution. Figure 9 shows a sequence of frames displaying the vorticity field during one period of the cylinder motion. The first and last frames correspond, respectively, to the lower and upper extreme positions of the cylinder while the middle frame corresponds to the mean cylinder location. The vortices in the wake of the oscillating cylinder have a larger lateral dimension compared to those in the wake of a fixed cylinder. The solution was computed on CRAY-XMP-EA. The linear equation system resulting from the finite element discretizations is solved using the

GMRES method in conjunction with CEBE preconditioner [10]. An average cluster size of 23 elements and a Krylov space of dimension 25 was used for the computations.

Reynolds number 300

At Reynolds number 300 the reduced natural frequency of the spring-mass system is larger than the Strouhal number for flow past a fixed cylinder. Initially, the oscillator exhibits the phenomenon of beats. At a later time, the vortex shedding frequency of the cylinder locks on to the natural frequency of the spring-mass system. Finally the cylinder reaches a periodic oscillation amplitude of approximately one radius. Figure 10 shows the time histories of the drag and lift coefficients and the normalized vertical displacement of the cylinder when it reaches a temporally periodic state. Figure 11 shows a sequence of frames displaying the vorticity field during one period of the cylinder motion. The first and last frames correspond, respectively, to the lower and upper extreme positions of the cylinder while the middle frame corresponds to the mean cylinder location. In this case, the longitudinal spacing between the vortices in the wake of the cylinder is smaller than that for a fixed cylinder. This arrangement of vortices appears to be unstable and therefore the vortices coalesce downstream. These computations were carried out on CM-5. The linear equation system is solved using GMRES in conjunction with a diagonal preconditioner. The dimension of the Krylov space used is 30.

Flow past a stationary NACA 0012 airfoil at Reynolds number 100,000

Unsteady laminar solution is computed for flow past a stationary NACA 0012 airfoil at 10° angle of attack. The Reynolds number, based on the chord length of the airfoil and the free-stream velocity, is 100,000. The finite element mesh employed for this simulation consists of 26,900 nodes and 26,600 quadrilateral elements. The airfoil of unit chord length is located at (0,0). The computational domain lies in a rectangular box whose bottom left and top right coordinates are (-6,-6) and (20,6), respectively. The time step is 0.002. A uniform inflow velocity of 1.0 is specified at the left boundary. The right boundary is an outflow boundary, and traction-free condition is applied there. Symmetry conditions at the lower and upper boundaries and the no-slip condition at the airfoil surface are specified. At each time step approximately 160,000 equations are solved using the GMRES method in conjunction with a diagonal preconditioner. The dimension of the Krylov vector space employed is 50. These computations were carried out on CM-5.

Figure 12 shows, respectively, a sequence of frames displaying the vorticity field and stream function at five different instants. From these pictures, it can be observed that the flow on the upper surface of the airfoil separates very close to the leading edge. Our computations do not reveal any apparent periodicity in the shedding of the vortex structures. This fact also manifests itself in the time histories of the lift and drag coefficients on the airfoil which are shown in Figure 13. We do realize that, in reality, flows at such high Reynolds numbers are turbulent. Our goal here is to demonstrate that our formulations are robust enough to handle numerical challenges posed by such high Reynolds number flows.

Flow past a freely falling NACA 0012 airfoil

This simulation involves a NACA 0012 airfoil falling under the action of gravity and fluid forces. The airfoil is assumed to be made of a material with density of 50. The density of the surrounding fluid is 1. Based on the density and the shape of the airfoil its mass and polar moment of inertia are, respectively, 4.068 and 0.224. The center of gravity of the airfoil lies at 0.417 chord lengths from the leading edge. The airfoil of unit chord length is initially located at (0,0). The computational domain lies in a rectangular box whose bottom left and top right coordinates are (-10,-10) and (20,10), respectively. The gravitational force, of magnitude 1.0, acts in the negative x-direction. The finite element mesh employed for this simulation consists of 8,446 nodes and 8,304 elements. Zero velocity is specified at the left and the top boundaries. At the lower boundary, second component (the component normal to the lower boundary) of velocity is specified a zero value, while the other component is free. Traction free boundary conditions are specified at the right boundary. The viscosity of the fluid is 0.01. The time step is 0.025.

At $t = 0$, the airfoil is released from rest at a 10° angle from the line of gravity. Figure 14 shows the time histories of the forces, velocities and the displacements associated with the airfoil. The pitch rate and the displacement are in degrees/unit time and degrees, respectively; the linear velocities and displacements are reported for the mid-chord point of the airfoil. We observe from the figure that the airfoil reaches a temporally periodic solution. In addition to having a linear velocity, there is a superimposed pitching motion. Figure 15 shows a sequence of frames of the vorticity field at various instants during one pitch cycle of the airfoil. The frames in the left column show the global vorticity fields; the close-ups around the airfoil are displayed in the right column. In our computations, we move the mesh with the velocity of the mid-chord point of the airfoil. The pitching motion of the airfoil is accommodated by moving the nodes according to a scheme described in [5]. It should be noted that this problem involves very large displacements of the airfoil; despite that, we are able to carry out the computations without remeshing. These results were computed on CM-5.

Flow past a "projectile"

In this problem we simulate the dynamics of a "projectile". The projectile is modeled by a two dimensional, missile-like object. The nose section of the projectile, one-fifth of the chord, is a half ellipse. The remaining part of the object is a rectangle with rounded off corners. The maximum thickness of the projectile is 12 percent of the chord. The finite element mesh used for this problem is very similar to the one in the previous problem. The density of the nose is 1,000 while that of the rest of the object is 50. The density of the surrounding fluid is 1. The mass and polar moment of inertia are, respectively, 23.64 and 1.23. The center of gravity of the projectile lies at 0.21 chord lengths from the leading edge. The gravity force, of magnitude 0.005, acts in the negative y direction. Zero velocity is specified at the left boundary. At the lower and upper boundaries second component (the component normal to the boundary) of velocity is specified a zero value. Traction free boundary conditions are specified at the right boundary. The viscosity of the fluid is 0.001. The time step used is 0.025.

The initial condition for this simulation is the unsteady solution for flow past the projectile which is being towed at a 10° angle of attack in the negative x direction at a speed of 1.0. Then the projectile is released. Figure 16 shows the time histories of the forces, velocities and the displacements of the projectile. The pitch rate and displacement are in degrees/unit time and degrees, respectively; the linear velocities and displacements are reported for the midchord point of the projectile. Figure 17 shows a sequence of frames of the vorticity field and stream function at various instants during the computation. From the figures we observe that as the simulation progresses the magnitude of the vertical component of velocity increases while that of the horizontal component decreases. As expected, the overall speed of the projectile decreases. Also, the pitch displacement of the projectile increases with time but the angle of attack stays at a value close to zero. This fact can be observed from the stream function pictures.

Flow past a cylinder at Reynolds number 5,000

The velocity-pressure-stress formulation is used to compute flow past a fixed cylinder in two dimensions, at Reynolds number 5,000. The upper and lower boundaries are flow symmetry lines, while the downstream boundary is traction-free. The mesh consists of 21,408 quadrilateral elements, with continuous bilinear interpolation functions for all variables. The element size near the cylinder surface is of the order 0.01. A time step size of 0.1 was selected to provide sufficient resolution of the

vortex shedding periods. A diagonal scaling with no preconditioning was applied to the system. The Krylov subspace size is 50, with 5 outer GMRES iterations, and, typically, 4 non-linear iterations per time step. The simulation was continued for 2,080 time steps after restart from a steady-state solution at Reynolds number 100, and reached a periodic state with Strouhal number 0.256, near $t = 100.0$. This state is characterized by a downward deflection of the vortex street, and non-zero positive mean value of the lift coefficient. The presence of two distinct periodic solutions at this Reynolds number was confirmed by numerically inverting, at $t = 160.0$, the entire flow field about the horizontal line passing through the center of the cylinder. The resulting upward deflection of the wake continued unperturbed, proving that the two solutions (upward and downward biased) are equally admissible by the system.

Four different vorticity fields are shown in Figure 18. The four frames represent the fully developed periodic flow field, at an instant when the lift coefficient attains the maximum, mean and minimum and subsequent mean values, respectively. The entire time history of the drag and lift coefficients is shown in Figures 19 and 20.

The performance measurements taken for this problem revealed the total computation speed of 560 megaflops on CM-200 computer with 32,768 processors. This figure includes parallel output of data to the DataVault mass storage system. In the solution phase the speed of communication-bound GMRES solver routine applied to the system with 129,610 degrees of freedom was 520 megaflops. On the other hand, the highly parallel matrix formation phase achieved 1,610 megaflops on the same machine. All computations were performed in double (64-bit) precision.

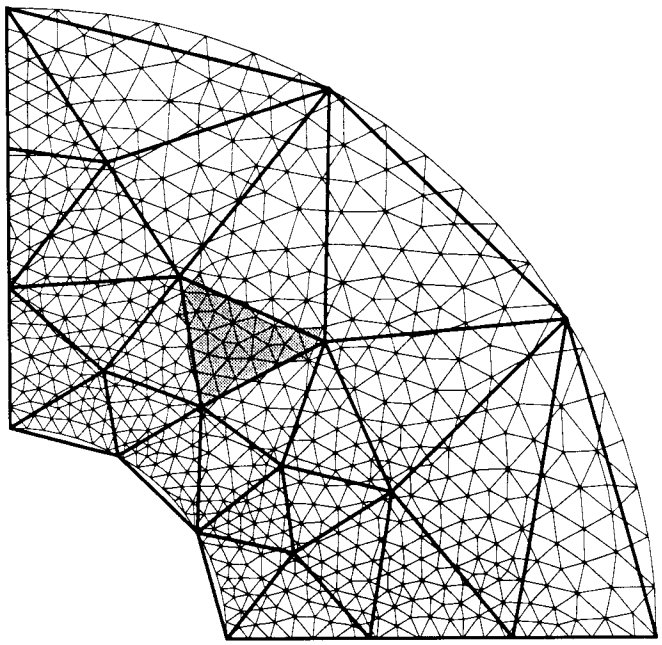

Figure 1. The CEBE/CC strategy for totally unstructured meshes: the fine (primary) and coarse (companion) meshes and the cluster of elements associated to a typical element of the coarse mesh.

REFERENCES

[1] T.J.R. Hughes, L.P. Franca, and G.M. Hulbert, "A new finite element formulation for computational fluid dynamics: VIII. the Galerkin/least-squares method for advective-diffusive equations", *Computer Methods in Applied Mechanics and Engineering*, **73** (1989) 173–189.

[2] T.E. Tezduyar, S. Mittal, S.R. Ray, and R. Shih, "Incompressible flow computations with stabilized bilinear and linear equal-order-interpolation velocity-pressure elements", *Computer Methods in Applied Mechanics and Engineering*, **95** (1992) 221–242.

[3] T.E. Tezduyar, M. Behr, and J. Liou, "A new strategy for finite element computations involving moving boundaries and interfaces – the deforming-spatial-domain/space time procedure: I. The concept and the preliminary tests", *Computer Methods in Applied Mechanics and Engineering*, **94** (1992) 339–351.

[4] T.E. Tezduyar, M. Behr, S. Mittal, and J. Liou, "A new strategy for finite element computations involving moving boundaries and interfaces – the deforming-spatial-domain/space time procedure: II. Computation of free-surface flows, two-liquid flows, and flows with drifting cylinders", *Computer Methods in Applied Mechanics and Engineering*, **94** (1992) 353–371.

[5] S. Mittal and T.E. Tezduyar, "A finite element study of incompressible flows past oscillating cylinders and airfoils", Research Report UMSI 91/307, University of Minnesota Supercomputer Institute, 1200 Washington Avenue South, Minneapolis, MN 55415, December 1991, ~~to appear in~~ *International Journal for Numerical Methods in Fluids*. ← **15** (1992) 1073-1118.

[6] M. Behr, L.P. Franca, and T.E. Tezduyar, "Stabilized finite element methods for the velocity-pressure-stress formulation of incompressible flows", Research Report UMSI 92/8, University of Minnesota Supercomputer Institute, 1200 Washington Avenue South, Minneapolis, MN 55415, January 1992, ~~to appear in~~ *Computer Methods in Applied Mechanics and Engineering*.← **104** (1993) 31-48.

[7] M. Behr, A. Johnson, J. Kennedy, S. Mittal, and T.E. Tezduyar, "Computation of incompressible flows with implicit finite element implementations on the Connection Machine", Research Report UMSI 92/102, University of Minnesota Supercomputer Institute, 1200 Washington Avenue South, Minneapolis, MN 55415, April 1992. ← *Computer Methods in Applied Mechanics and Engineering, **108** (1993) 99-118.*

[8] Daniel R. Lynch, "Unified approach to simulation on deforming elements with application to phase change problems", *Journal of Computational Physics*, **47** (1982) 387–411.

[9] J. Liou and T.E. Tezduyar, "A clustered element-by-element iteration method for finite element computations", in R. Glowinski et al., editor, *Domain Decomposition Methods for Partial Differential Equations*, Chapter 13, pages 140–150, SIAM, 1991.

[10] J. Liou and T.E. Tezduyar, "Computation of compressible and incompressible flows with the clustered element-by-element method", Research Report UMSI 90/215, University of Minnesota Supercomputer Institute, 1200 Washington Avenue South, Minneapolis, MN 55415, October 1990. ← See update U1 below.

[11] T.E. Tezduyar, M. Behr, S.K. Abadi, S. Mittal, and S.E. Ray, "A new mixed preconditioning method for finite element computations", Research Report UMSI 91/160, University of Minnesota Supercomputer Institute, 1200 Washington Avenue South, Minneapolis, MN 55415, June 1991, ~~to appear in~~ *Computer Methods in Applied Mechanics and Engineering*. ← **99** (1992) 27-42.

Publication Update

U1. J. Liou and T.E. Tezduyar, "Clustered Element-by-Element Computations for Fluid Flow", Chapter 9 in *Parallel Computational Fluid Dynamics* (ed. H.D. Simon), MIT Press, Cambridge, Massachusetts (1992) 167-187.

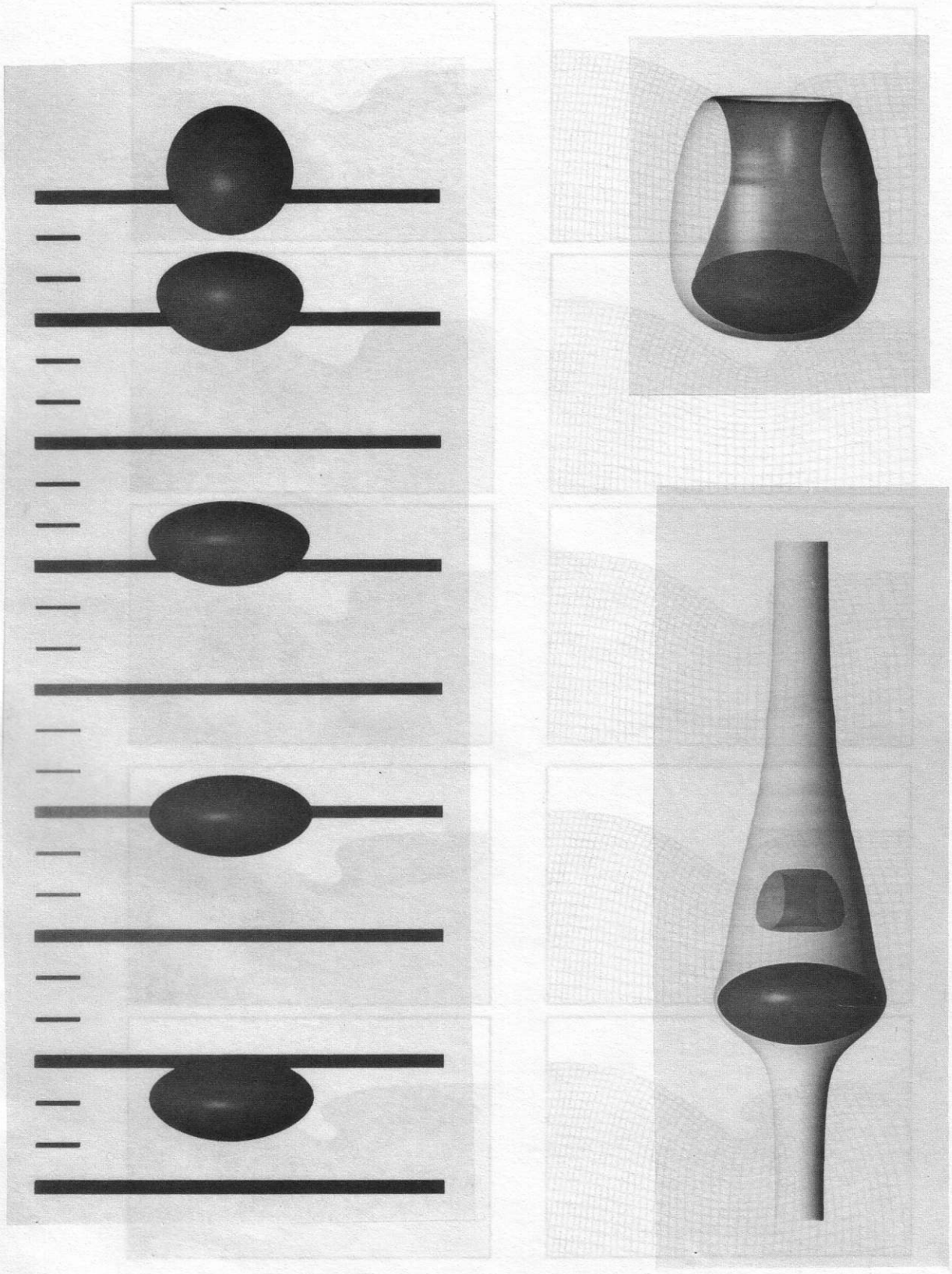

Figure 2. Falling viscous drop: shape (left), iso-surface of vorticity (right top) and iso-surfaces of stream function (right bottom) at terminal velocity.

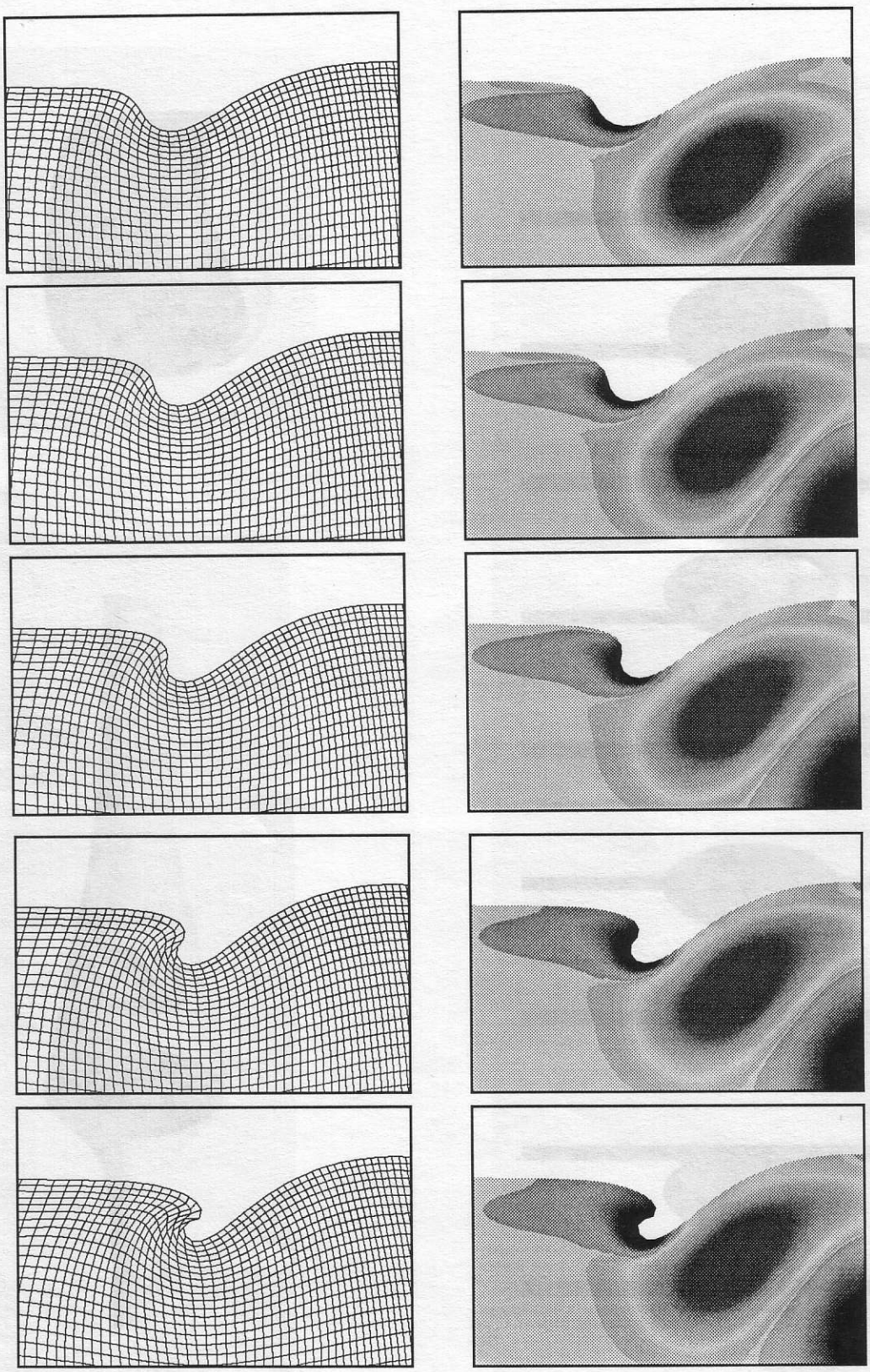

Figure 3. Vortex interaction with a free surface: mesh (left) and vorticity (right) at different instants.

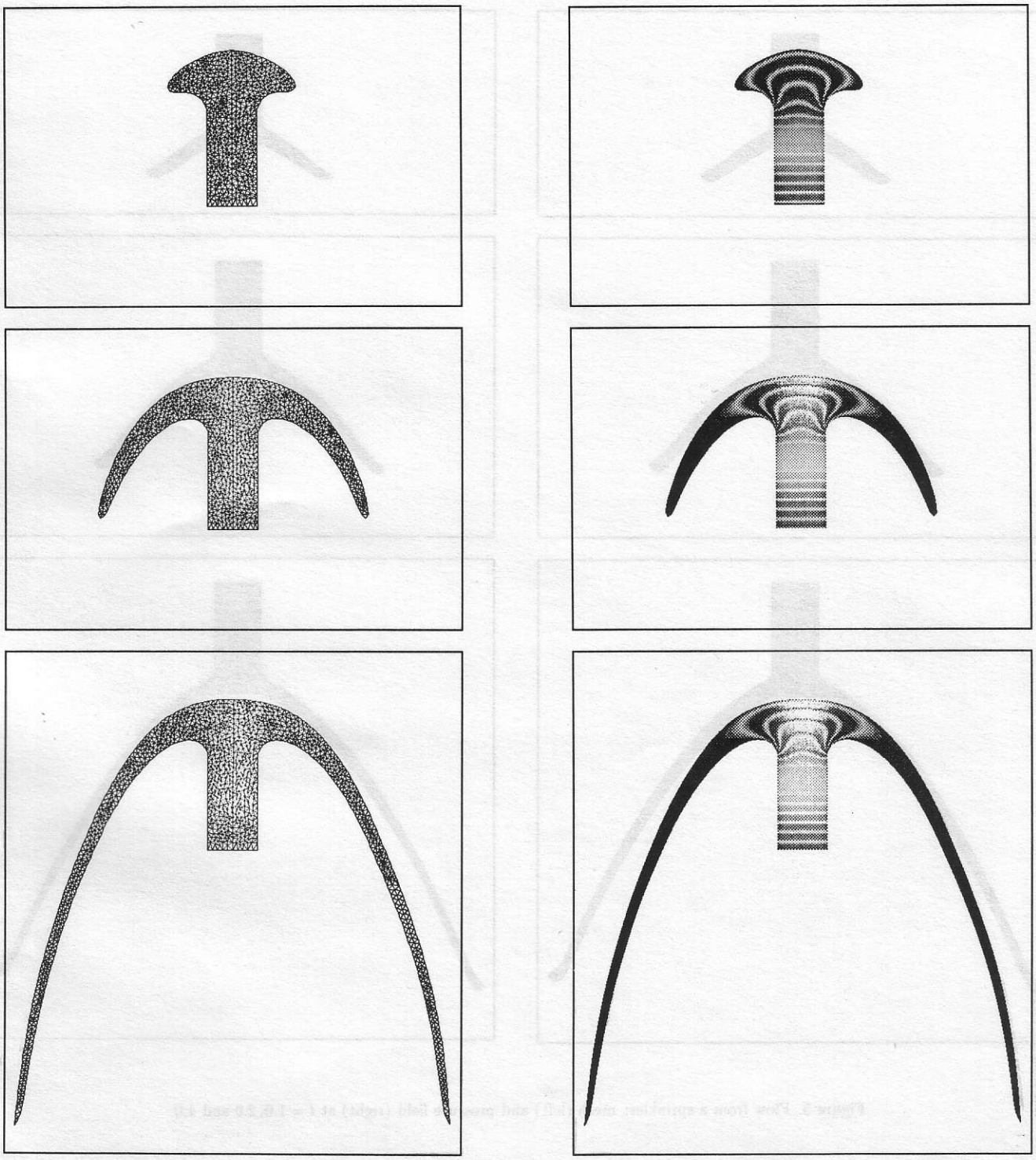

Figure 4. Flow from a fountain: mesh (left) and pressure field (right) at $t = 2.0, 4.0$ and 6.0.

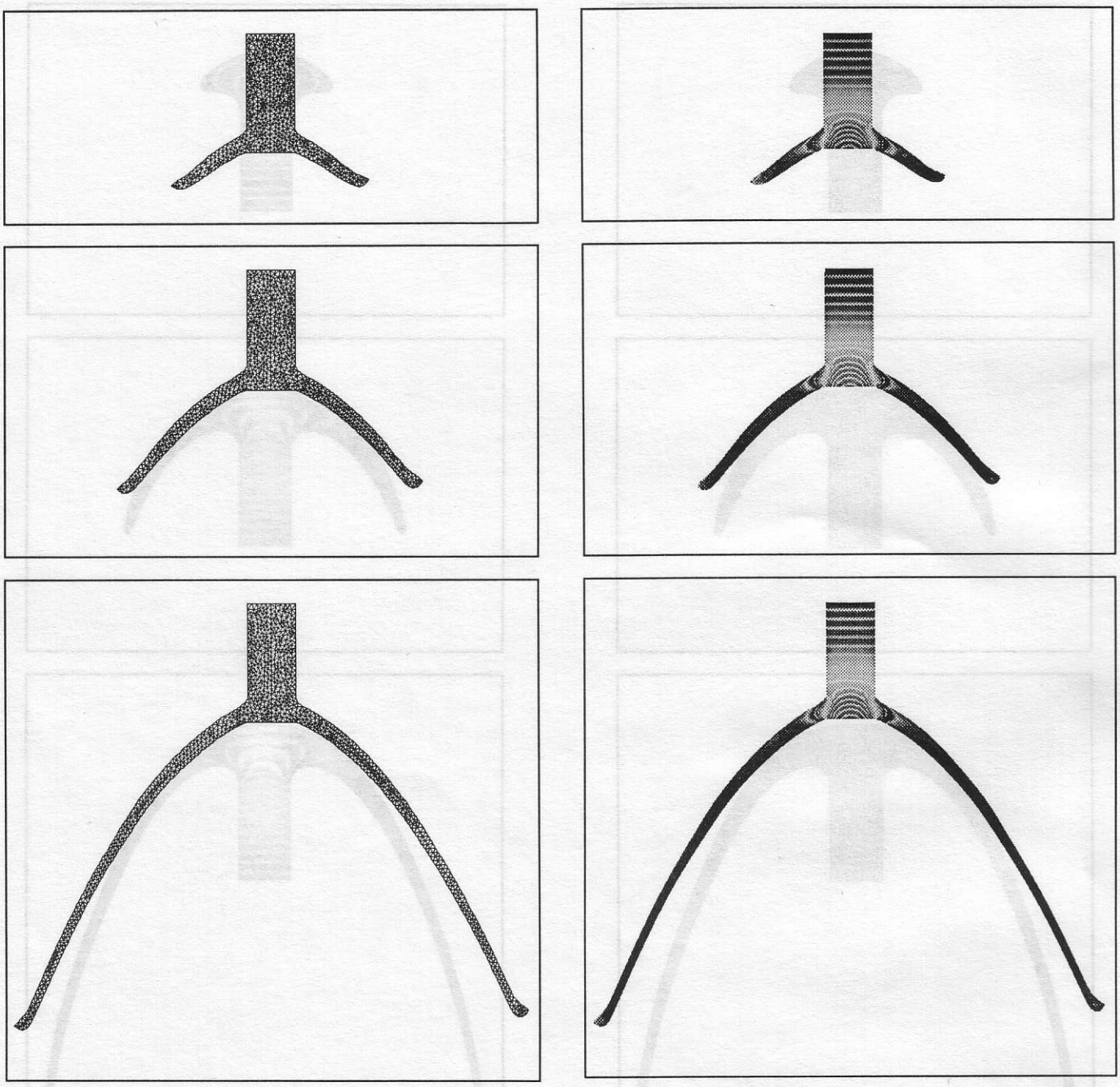

Figure 5. Flow from a sprinkler: mesh (left) and pressure field (right) at $t = 1.0, 2.0$ and 4.0.

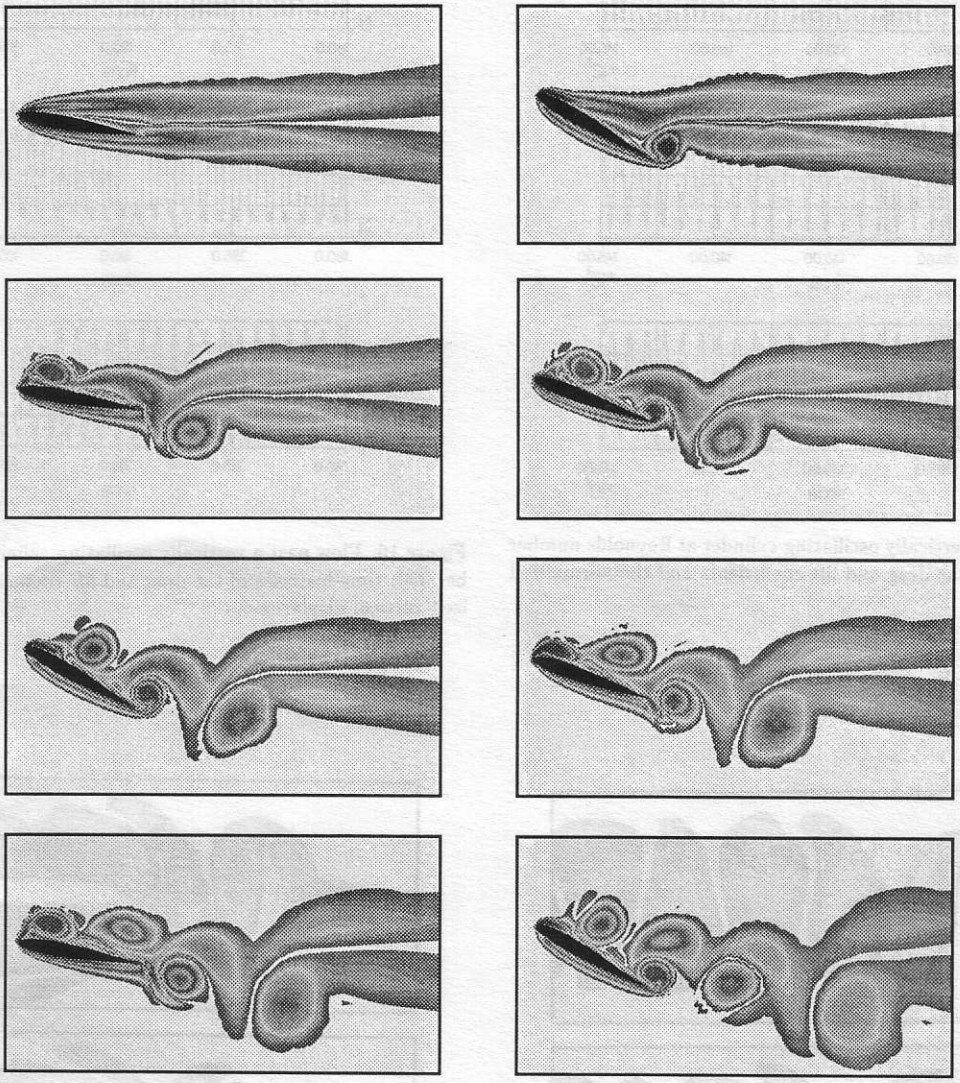

Figure 6. Flow past an oscillating NACA 0012 airfoil at Reynolds number 1,000: vorticity field evolution.

Figure 7. Flow past an oscillating NACA 0012 airfoil at Reynolds number 1,000: mesh at 10° and 30° angle of attack.

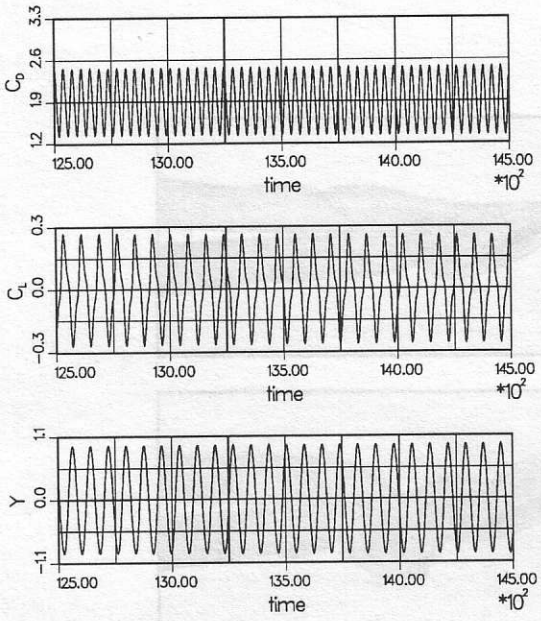

Figure 8. Flow past a vertically oscillating cylinder at Reynolds number 324: time histories of the drag and lift coefficients and the normalized vertical displacement.

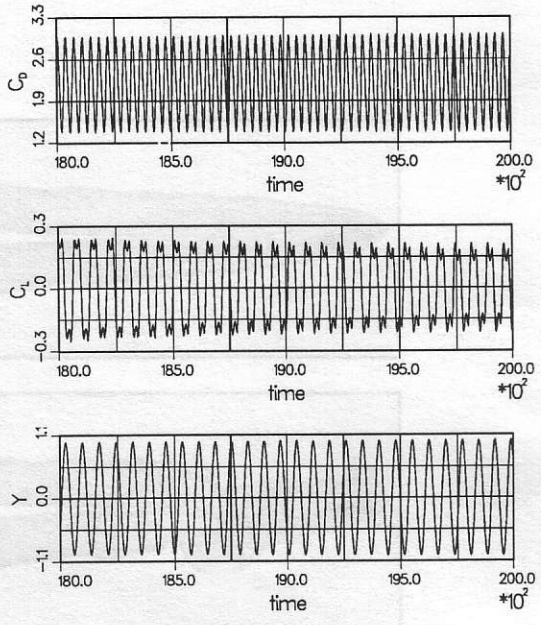

Figure 10. Flow past a vertically oscillating cylinder at Reynolds number 300: time histories of the drag and lift coefficients and the normalized vertical displacement.

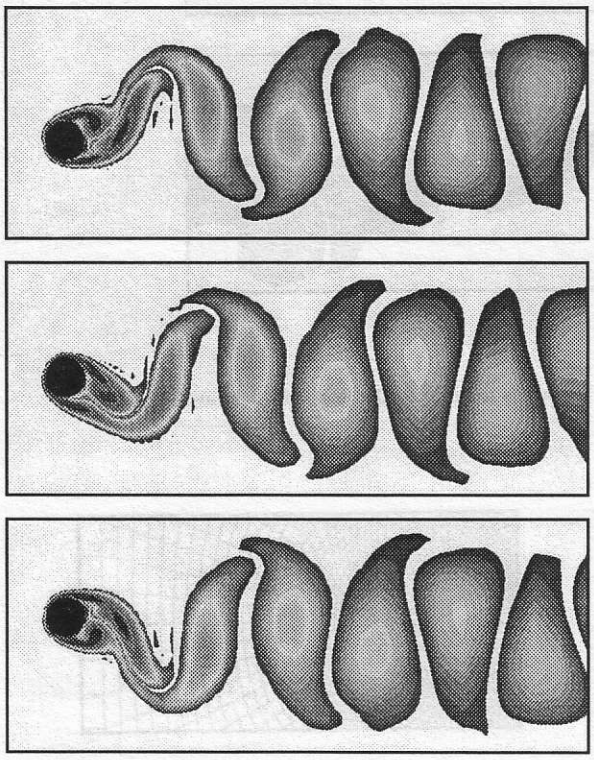

Figure 9. Flow past a vertically oscillating cylinder at Reynolds number 324: vorticity at the lowest, mean and highest location of the cylinder.

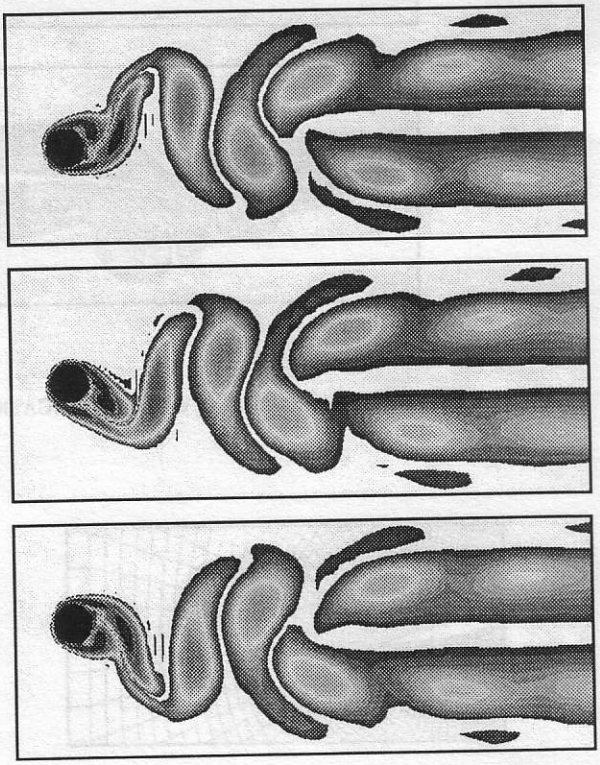

Figure 11. Flow past a vertically oscillating cylinder at Reynolds number 300: vorticity at the lowest, mean and highest location of the cylinder.

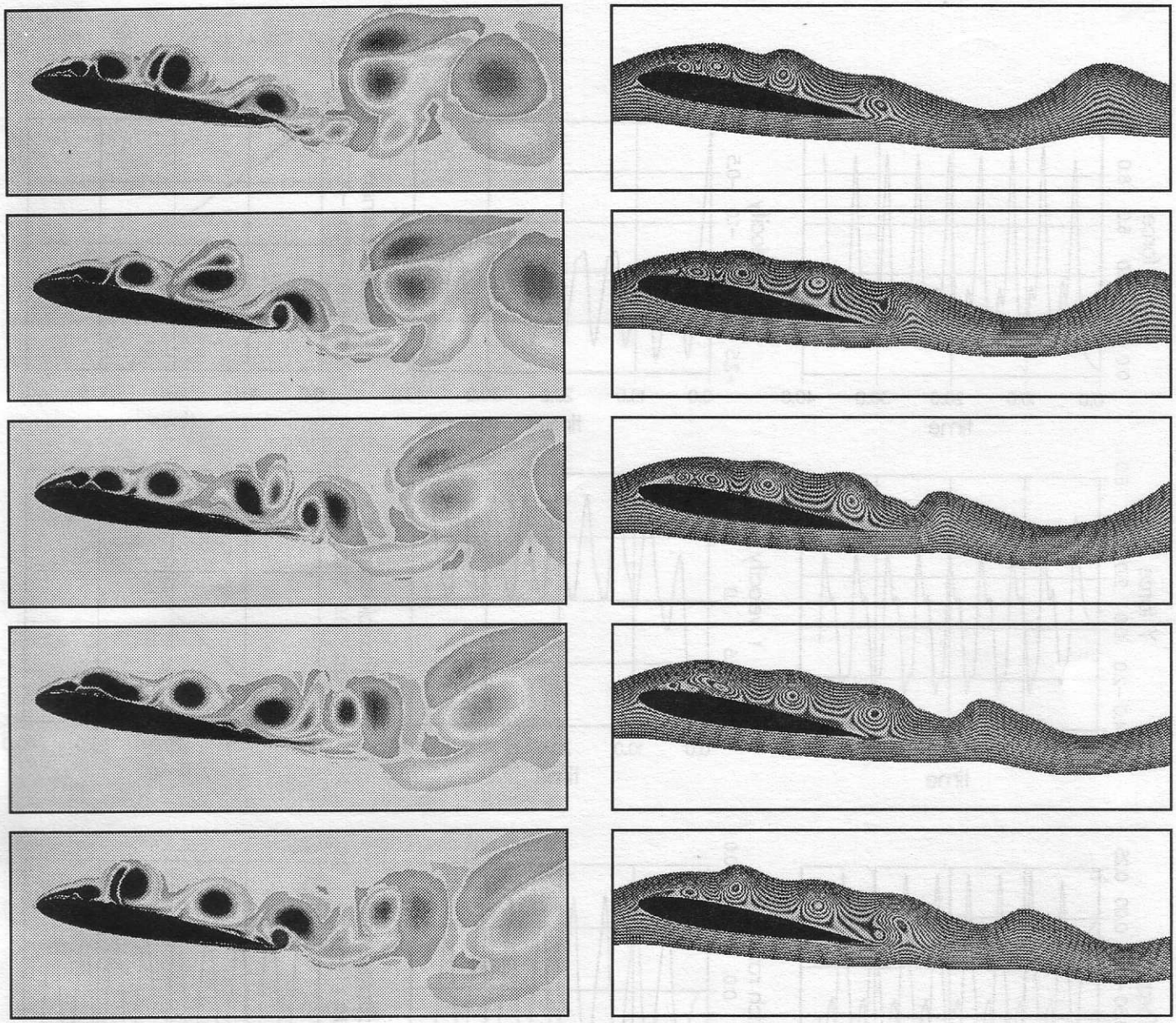

Figure 12. Flow past a fixed NACA 0012 airfoil at Reynolds number 100,000: vorticity (left column) and streamlines (right column) at $t = 14.4, 14.6, 14.8, 15$ and 15.2.

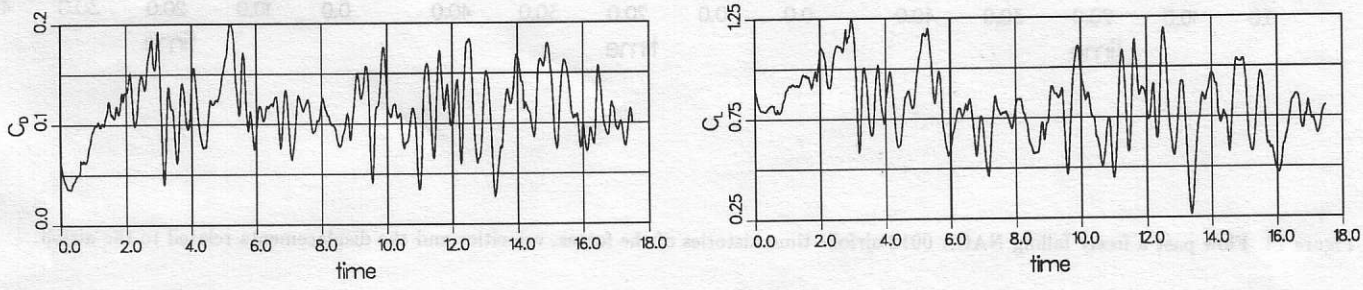

Figure 13. Flow past a fixed NACA 0012 airfoil at Reynolds number 100,000: time histories of the lift and drag coefficients.

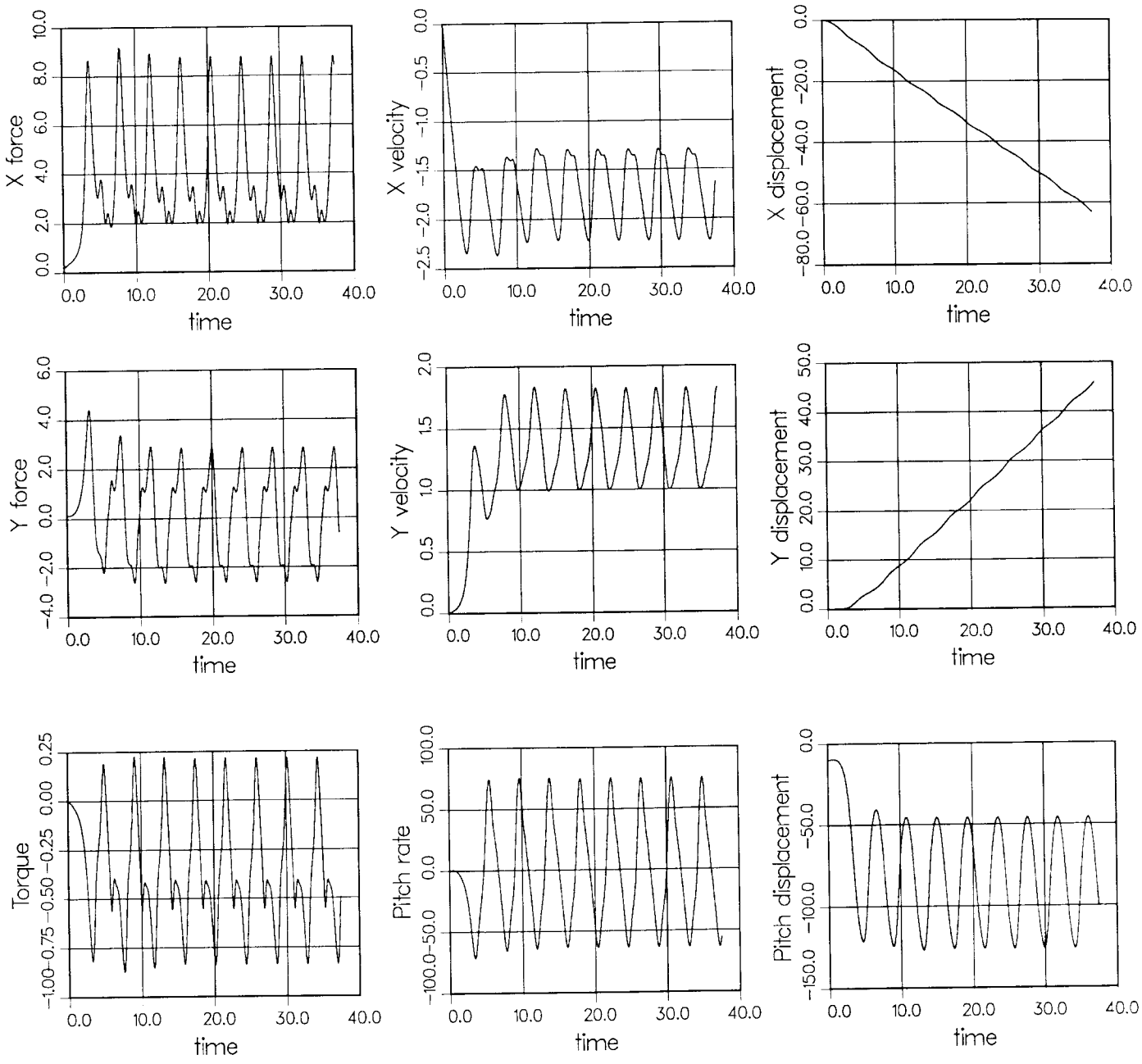

Figure 14. Flow past a freely falling NACA 0012 airfoil: time histories of the forces, velocities and the displacements related to the airfoil.

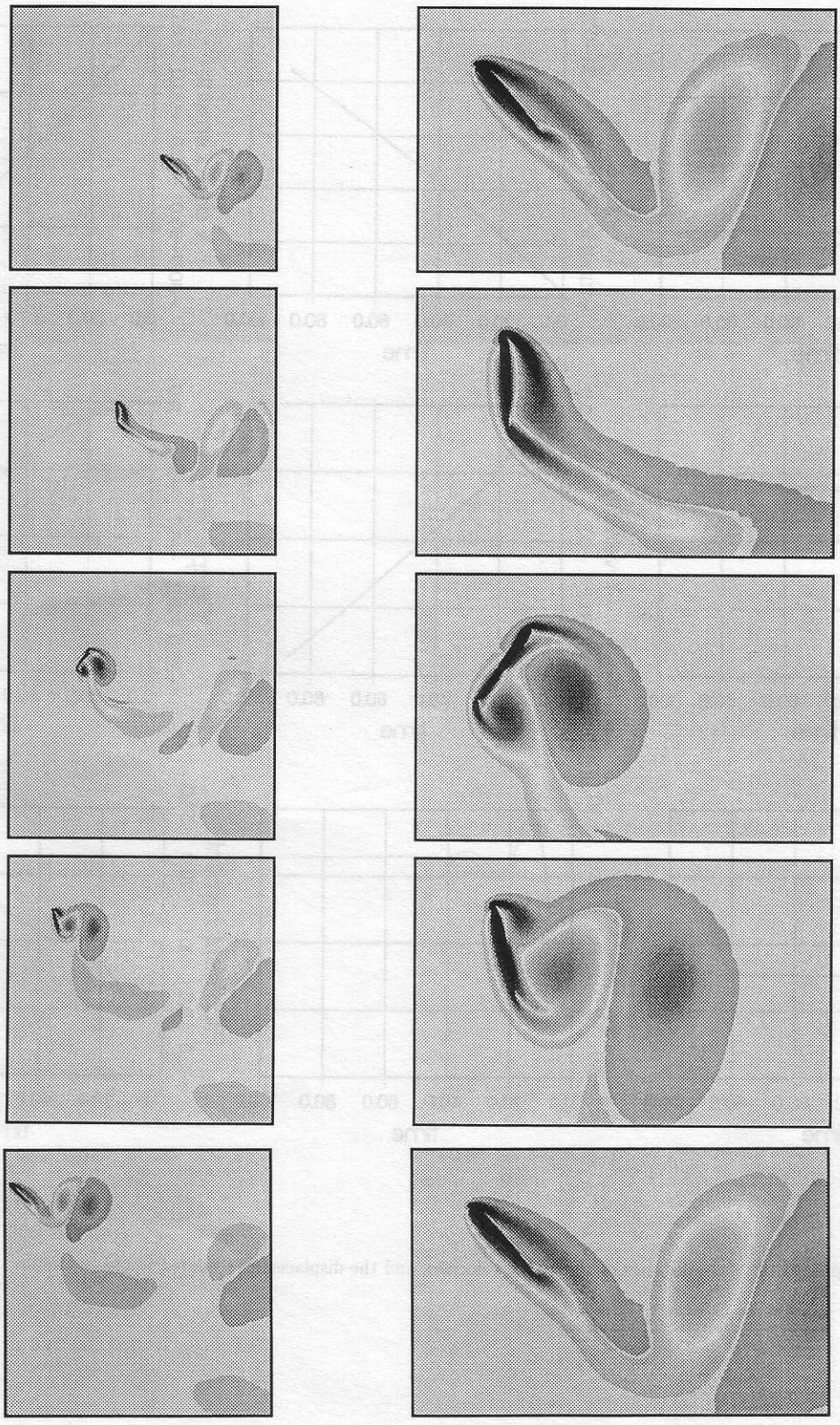

Figure 15. Flow past a freely falling NACA 0012 airfoil: vorticity at various instants during one pitch cycle of the airfoil.

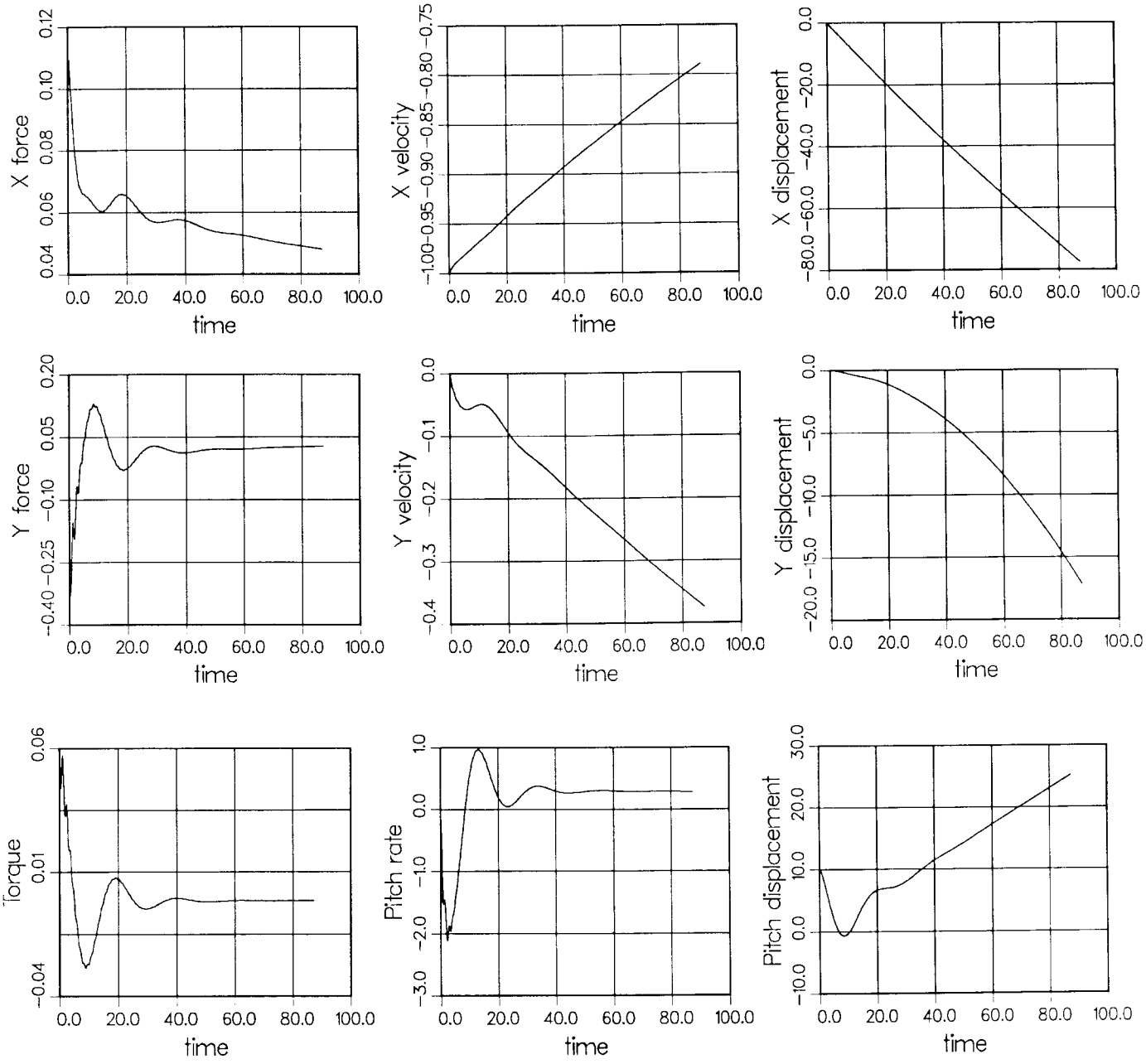

Figure 16. Flow past a "projectile": time histories of the forces, velocities and the displacements related to the projectile.

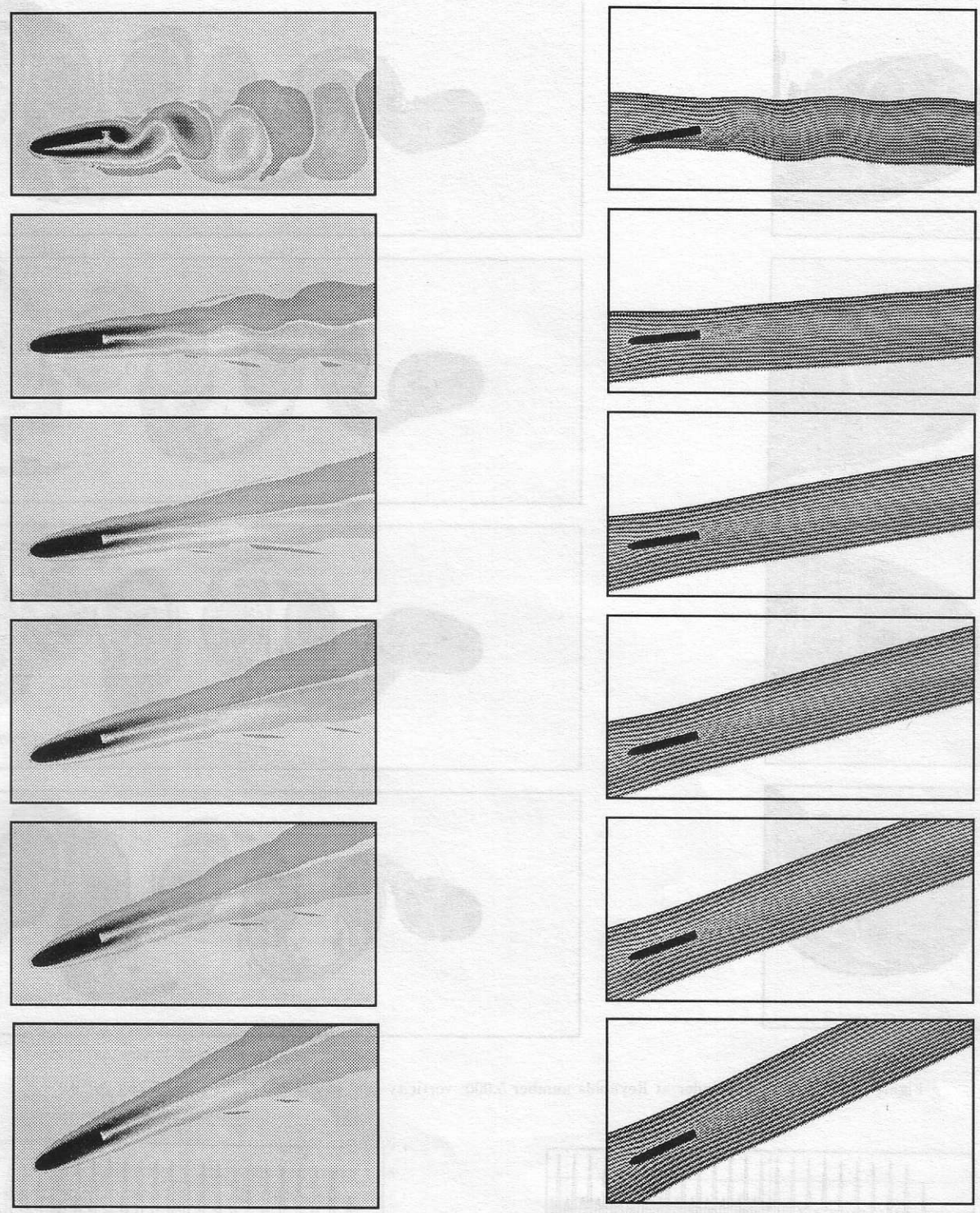

Figure 17. Flow past a "projectile": vorticity (left column) and stream function (right column) at $t = 0.0, 17.5, 35.0, 52.5, 70.0$ and 87.5.

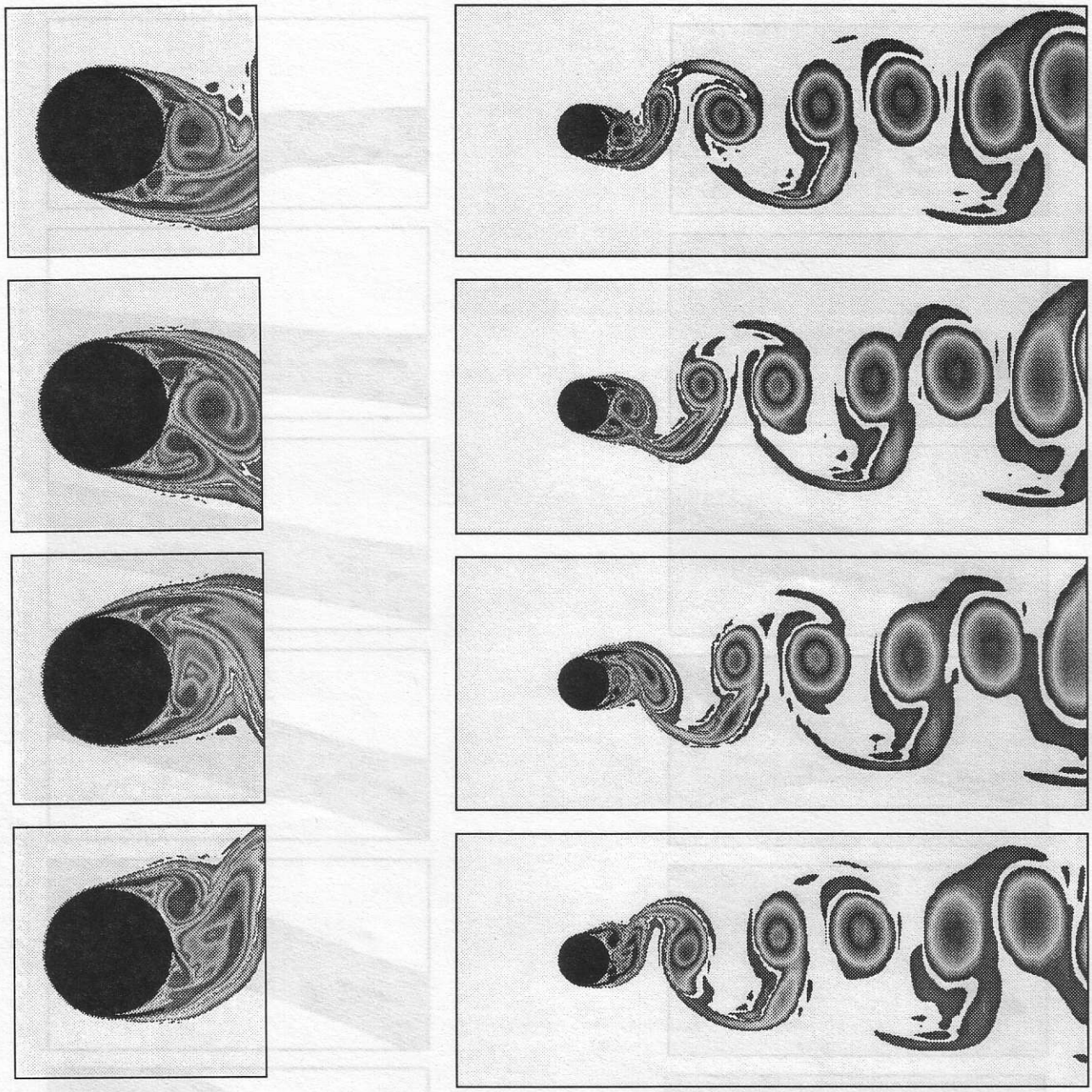

Figure 18. Flow past a cylinder at Reynolds number 5,000: vorticity field at $t = 200.1, 202.4, 204.0$ and 205.9.

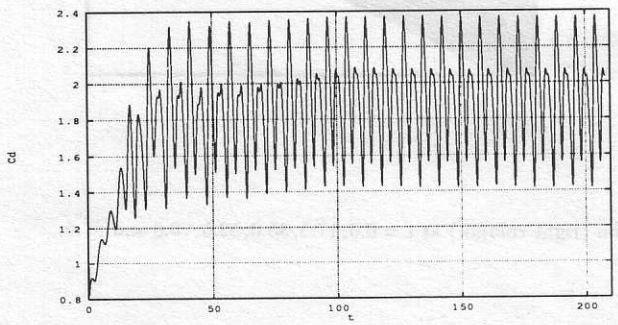

Figure 19. Flow past a cylinder at Reynolds number 5,000: time history of the drag coefficient.

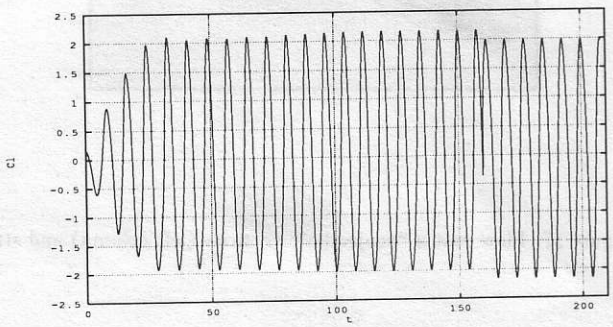

Figure 20. Flow past a cylinder at Reynolds number 5,000: time history of the lift coefficient.